ChemComm

Chemical Communications

Accepted Manuscript

Volume 54
Number 1
4 January 2018
Pages 1-112

ChemComm
Chemical Communications
rsc.li/chemcomm

COMMUNICATION
S. J. Connon, M. O. Senge et al
Conformational control of nonplanar free base porphyrins: towards bifunctional catalysts of tunable basicity

ISSN 1359-7345

ROYAL SOCIETY
OF CHEMISTRY

This is an Accepted Manuscript, which has been through the Royal Society of Chemistry peer review process and has been accepted for publication.

Accepted Manuscripts are published online shortly after acceptance, before technical editing, formatting and proof reading. Using this free service, authors can make their results available to the community, in citable form, before we publish the edited article. We will replace this Accepted Manuscript with the edited and formatted Advance Article as soon as it is available.

You can find more information about Accepted Manuscripts in the Information for Authors.

ROYAL SOCIETY
OF CHEMISTRY

rsc.li/chemcomm

COMMUNICATION

Polyoxometalate-incorporated NiFe-based oxyhydroxides for enhanced oxygen evolution reaction in alkaline media

Yuyan Qiao[‡ a,b,c], Yanqiu Pan[‡ c], Wenjun Fan[*a], Guifa Long[*d] and Fuxiang Zhang[*a]

NiFe-based oxyhydroxides are promising electrocatalysts for the oxygen evolution reaction (OER) in alkaline media, but further enhancing their OER performance remains a significant challenge. Herein, we in situ incorporated polyoxometalates into NiFe oxyhydroxide to form a homogeneous/heterogeneous hybrid material, which induces the electronic interaction between Ni, Fe and Mo sites, as revealed by a variety of characterizations and theoretical calculations. The resulting hybrid electrocatalyst delivers a low overpotential of 203 mV at 10 mA cm^{-2} and a TOF of 2.34 s^{-1} at 1.53 V in alkaline media. This work presents a critical step towards developing high-performance OER catalysts by constructing metal-POM hybrids.

Solar-to-hydrogen conversion through electrochemical water splitting is a promising technology for utilizing renewable energy resources.[1, 2] However, the overall efficiency of water splitting is hampered by the sluggish kinetics of anodic oxidation evolution reaction (OER). Although IrO$_2$ and RuO$_2$ have shown promising catalytic activity for OER, the scarcity and high costs remain major obstacles to their large-scale applications.[3, 4] Enormous strategies have been developed to optimize the catalytic performance of OER electrocatalyst.[5, 6] The catalytic activity can be modified by designing nanostructured electrocatalyst,[7] heteroatom doping,[8] strain effect,[9] and defect engineering.[10] The stability of catalysts can be improved by in situ growing catalysts on conductive substrates,[11] synthesizing carbon composites catalysts,[12] or incorporating the stabilizer,[13] etc. Despite significant advancements in this field, the development of non-precious metal electrocatalysts with high activity and stability remains a formidable challenge.

Among the critical factors contributing to this challenge are low intrinsic activity and limited utilization of active sites. By contrast, homogeneous catalysts, with their tunable structures at the molecular level, exhibit ultrahigh intrinsic activity.[14, 15] However, the poor stability and recyclability dramatically hinder their practical application. Thus, constructing efficient and stable catalysts by leveraging the advantages of both homogeneous and heterogeneous catalysts is highly desired.[16] Polyoxometalate (POM)-based materials, with rich redox chemistry and tunable structures, have attracted widespread attention as potential candidates in electrocatalysis.[17] Typically, phosphomolybdic acid (H$_3$PMo$_{12}$O$_{40}$, PMA) has a classical Keggin structure with 36 oxygen atoms exposed and is an ideal platform for anchoring sites.[18] The POM-based materials have been verified as promising molecular water oxidation catalysts in close-to-neutral pH conditions.[19] Nevertheless, POM-based compounds face the problem of poor stability and conductivity in electrochemical processes. To address this, heterogenization of POM with conductive substrates or constructing electron transfer between the POM matrix and the active sites is urgently necessary for accelerating the OER process and increasing the stability.

Herein, by adopting the cluster-nuclei assembly strategy, we controllably synthesized carbon nanotubes (CNTs) supported hybrid NiFe oxyhydroxide-PMA catalyst (denoted as NiFe-PMA/CNTs) on carbon fiber paper (CFP) substrate for alkaline oxygen evolution reaction (OER). CNTs can control the morphology of catalysts, increasing the surface area of the electrode and accelerate the charge transfer between the electrode and catalysts. The preparation of the NiFe-PMA/CNTs/CFP electrode follows a two-step synthesis approach (Figure S1). Typically, CNTs were first *in situ* grown on CFP by chemical vapor deposition method to get CNTs/CFP

a.State Key Laboratory of Catalysis, iChEM, Dalian Institute of Chemical Physics, Chinese Academy of Sciences, Dalian, 116023, China. E-mail: wjfan@dicp.ac.cn; fxzhang@dicp.ac.cn

b.Jiangxi Province Engineering Research Center of Ecological Chemical Industry, Jiujiang University, Jiujiang, 332005, China.

c. School of Chemical Engineering, Dalian University of Technology, Dalian, 116024, China;

d.Guangxi Key Laboratory of Chemistry and Engineering of Forest Products, School of Chemistry and Chemical Engineering, Guangxi University for Nationalities, Nanning, 530008, China; E-mail: gflong@gxmzu.edu.cn

‡ The two authors contributed equally to this work.

† Electronic Supplementary Information (ESI) is available. Details of experiments and theoretical computations See DOI: 10.1039/x0xx00000x

electodes (Figure S2), on which PMA clusters were incorporated with inorganic $NiFeO_x$ by solvothermal method to get the target catalyst. For comparison, the control samples of CNTs supported $NiFeO_x$ (NiFe/CNTs), CNTs supported PMA (PMA/CNTs) or bare CNTs were prepared (See Supplementary Information for details).

The as-obtained NiFe-PMA/CNTs catalyst (Figure 1a) displays a typical three-dimensional nanostructure similar to that of the CNTs/CFP, which can potentially supply enormous tunnels for gas release. A closer look at the catalyst by transmission electron microscopy (TEM) and aberration-corrected high-angle annular dark field scanning transmission electron microscopy (AC HAADF-STEM) reveals the coverage of small nanoparticles/clusters on carbon nanotubes (Figure 1 inset, Figure1 b-c, Figure S3), indicating the tight connection between CNTs and the catalyst.[20] The lattice fringe with a spacing of 0.34 nm is ascribed to the (002) plane of graphite-2H (Figure1b), while no prominent lattice fringe assigned to the NiFe or PMA species could be found, suggesting the amorphous character of the catalyst. Consistent results can be found in the X-ray diffraction (XRD) patterns of the catalysts in Figure S4, where no signals of Ni(Fe)OOH or PMA can be detected in the XRD patterns for NiFe-PMA/CNTs. The homogeneous distribution of Ni, Fe, Mo, P and O elements was confirmed by the energy dispersive X-ray (EDX) elemental mapping (Figure 1d-1i). Furthermore, the elemental contents of transition metals for different electrocatalysts were examined by inductively coupled plasma-atomic emission spectroscopy (ICP-AES) and the ratio of Ni : Fe : Mo in NiFe-PMA/CNTs was determined to be 1 : 1 : 0.6 (Table S1). Fourier transform infrared (FTIR) spectra show that the characteristic

peaks assigned to PMA at 1070, 966, 869, 791 cm^{-1} are well preserved for the NiFe-PMA/CNTs electrocatalyst (Figure S5).[21] The shift of corresponding characteristic peaks verifies the strong interaction between PMA, carbon materials, and NiFe (oxy)hydroxide catalysts.

The chemical states of the NiFe-PMA/CNTs catalyst (Figure S6-7) were analyzed by X-ray photoelectron spectroscopy (XPS). The high-resolution spectrum of Fe $2p_{3/2}$ in NiFe/CNTs exhibits a prominent peak at 711.0 eV, corresponding to the Fe^{3+} species (Figure 2a). By contrast, the main peak of Fe $2p_{3/2}$ for NiFe-PMA/CNTs experiences a slightly negative shift of ~0.2 eV, suggesting the interaction between PMA and Fe element. A similar negative shift in the binding energy of Ni $2p_{3/2}$ can be found in NiFe-PMA/CNTs as compared with the NiFe/CNTs (Figure 2b). It is worth noting that Ni^{3+} (858.0 eV and 857.4 eV) peaks appear in the Ni 2p spectrum of these two samples, respectively, which is known to be beneficial for prompting the formation of intermediate species (∗OOH) for OER.[22] Accordingly, the binding energy of O 1s in NiFe-PMA/CNTs was found to be higher than that in PMA/CNTs (Figure 2c), suggesting the electron transfer from O to Ni and Fe sites, which is further supported by the theoretical calculation results (Figure 4).

The local coordination structure of the NiFe-PMA/CNTs electrocatalyst was further verified by X-ray absorption Fine structure (XAFS). For NiFe-PMA/CNTs, the Fe K-edge X-ray absorption near-edge structure (XANES) spectra exhibit similar absorption edge of NiFe-PMA/CNTs, NiFe/CNTs and Fe_2O_3, indicating that the oxidation state of catalysts is around +3 (Figure 2d). However, the Fe absorption edge in NiFe-PMA/CNTs is slightly lower than that of the NiFe/CNTs. This
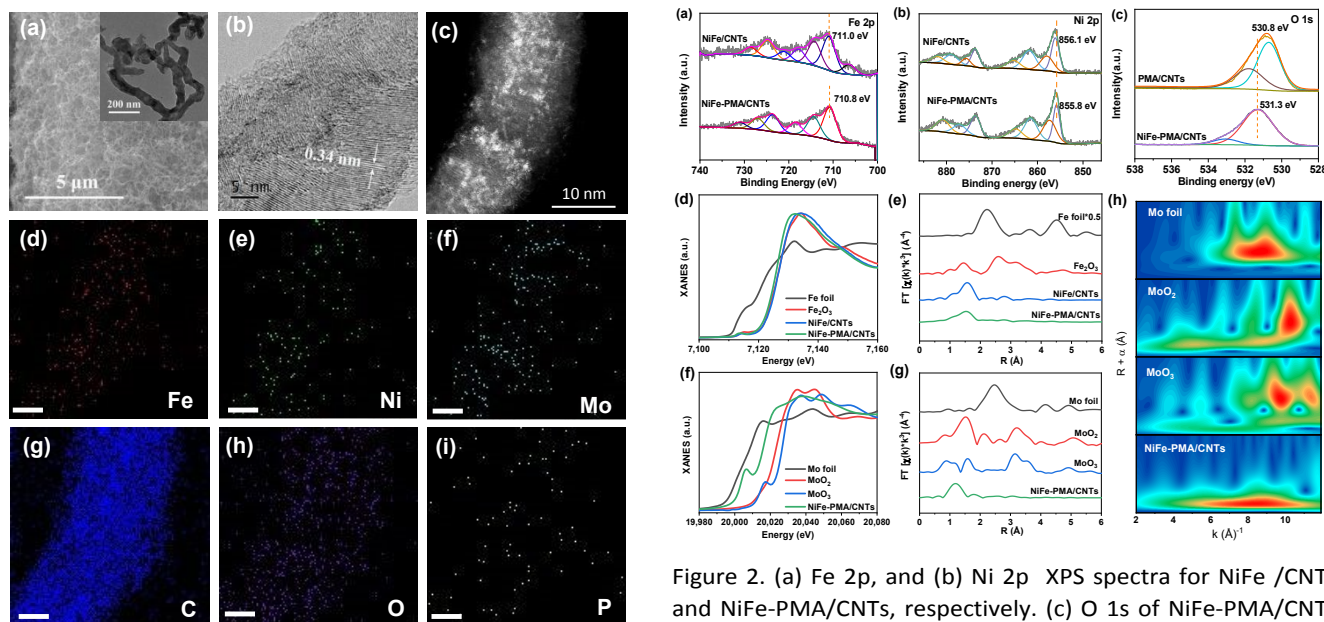
Figure 1. Morphological characterization of NiFe-PMA/CNTs. (a) SEM, inset shows the TEM of the catalyst, (b) HRTEM of one nanotube, (c) AC HAADF-STEM image of NiFe-PMA/CNTs, and (d-i) the corresponding EDX elemental mapping, Scale bar: 5 nm.

Figure 2. (a) Fe 2p, and (b) Ni 2p XPS spectra for NiFe /CNTs and NiFe-PMA/CNTs, respectively. (c) O 1s of NiFe-PMA/CNTs and PMA/CNTs. (d, f) Normalized K-edge XANES spectra, and (e, g) the corresponding k^3-weighted EXAFS spectra of NiFe/CNTs, NiFe-PMA/CNTs and reference samples for Fe and Mo (without phase correction), respectively. (h) Wavelet transform of the EXAFS for Mo foil, MoO_2, MoO_3, and NiFe-PMA/CNTs.

result suggests the prominent interaction between NiFe and PMA in which electrons are transferred from PMA to Fe, in accordance with the XPS result (Figure 2a, 2c). The Fourier transform extended XAFS (FT-EXAFS) curves in Figure 2e reveal the existence of Fe-O peak at about 1.5 Å (Figure 2e), which is further supported by the fitting results obtained from NiFe/CNTs and NiFe-PMA/CNTs (Figure S8, Table S2). The Mo K-edge absorption of NiFe-PMA/CNTs indicates the oxidation valence of Mo is between +0 and +4 (Figure 2f). The Mo-O coordination is validated by FT-EXAFS data and corresponding Wavelet transform (WT) (Figure 2g-h, Table S3) [23, 24].

The electrocatalytic OER activity of NiFe-PMA/CNTs was evaluated in 1 M KOH. Remarkably, NiFe-PMA/CNTs catalyst exhibits the highest catalytic OER activity as compared with the NiFe/CNTs catalyst and the other control samples (Figure 3a and Figure S9), underscoring the synergistic effect between PMA and $NiFeO_x$ species. Specifically, the overpotentials at 10 mA cm^{-2} and 50 mA cm^{-2} reach 203 mV and 246 mV for NiFe-PMA/CNTs catalyst (Figure 3b), respectively. When considering all metals as active sites, the TOF value of NiFe-PMA/CNTs catalyst at 1.53 V (vs RHE) is 2.34 s^{-1}, also superior to NiFe/CNTs (0.20 s^{-1}) and PMA/CNTs (0.03 s^{-1}). Notably, the high OER activity of NiFe-PMA/CNTs catalyst surpasses most non-noble metal electrocatalysts in alkaine solution (Table S4). The high OER activity is also reflected by the much lower Tafel slope (Figure 3c), revealing the fast reaction kinetics.

To investigate the effect of PMA on the catalytic activity of NiFe-PMA/CNTs, the double layer capacitance (C_{dl}) and the electrochemically active surface areas (ECSA) were evaluated. As shown in Figure S10, the calculated C_{dl} value of NiFe-PMA/CNTs is 29.8 mF cm^{-2}, which is smaller than that of NiFe/CNTs (C_{dl} = 50.0 mF cm^{-2}), indicating the higher intrinsic activity of NiFe-PMA/CNTs (Figure 3d). The Nyquist plots at 1.48 V 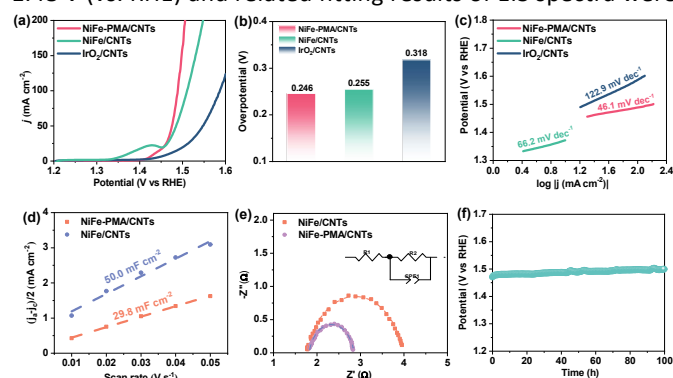(vs. RHE) and related fitting results of EIS spectra were applied to compare the interface kinetics of comparative samples (Figure 3e and Table S5). NiFe-PMA/CNTs showed relatively lower interface charge transfer resistance (R_{ct} = 1.0 Ω) than that of NiFe-C/CNTs (R_{ct} = 2.2 Ω), suggesting its enhanced interface kinetics.

To further evaluate the long-term stability of NiFe-PMA/CNTs, chronopotentiometric (CP) measurements were carried out at 10 mA cm^{-2} in 1.0 M KOH electrolyte. As depicted in Figure 3f, the overpotential exhibits marginal change during 100 h test, demonstrating excellent stability for NiFe-PMA/CNTs. During this process, the Faradaic efficiency of NiFe-PMA/CNTs electrocatalyst was around 100% (Figure S11), indicating the pure water oxidation reaction process. Additionally, the metal content in the electrolyte after electrochemical reaction (Table S6) shows insignificant change and thus manifests the robustness of the NiFe-PMA/CNTs catalyst. In comparison, NiFe/CNTs also show comparative stability for 100 h (Figure S12). Based the analysis of such characterizations as SEM, TEM, XRD and XPS before and after stability, NiFe-PMA/CNTs and NiFe/CNTs have non-considerable changes about the structures and compositions (Figure S13-16).

To further clarify the interaction of PMA and NiFe in NiFe-PMA-CNTs catalyst, density functional theory (DFT) calculations were performed. The calculation model was built based on the experimental characterizations. The optimized structures of PMA/CNTs, NiFe/CNTs and NiFe-PMA/CNTs are shown in Figure S17 and Figure 4a. The electronic structure of NiFe-PMA/CNTs catalyst was studied by the differential charge density (Figure 4b). It is revealed that electrons move from

Figure 3. (a) LSV polarization curves of NiFe-PMA/CNTs, NiFe/CNTs, and IrO$_2$ in 1 M KOH. (b) OER overpotentials at 50 mA·cm^{-2} for the various electrocatalysts in 1 M KOH. (c) Tafel plots of NiFe-PMA/CNTs, NiFe/CNTs, and IrO$_2$ in 1 M KOH. (d) Plots of current densities at 0.1 V (vs. Hg/HgO) versus scan rates of typical samples, respectively. (e) Nyquist plots of typical samples in 1 M KOH at 1.48 V (vs RHE) with the frequency range from 0.1 to 100 KHz. (f) Chronopotentiometry curve of NiFe-PMA/CNTs at 10 mA·cm^{-2} in 1 M KOH.
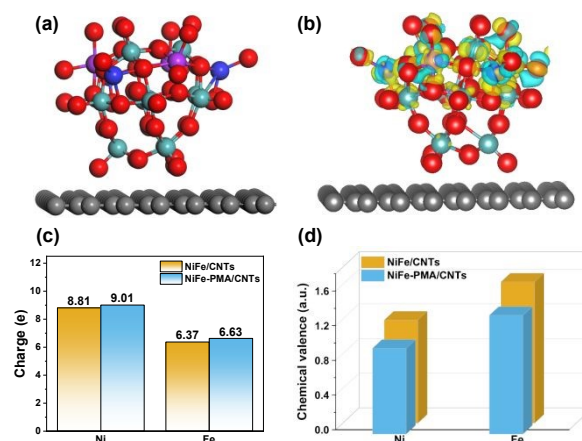

Figure 4. (a) Optimized structures of NiFe-PMA/CNTs catalyst. The balls in grey, red, pink, blue, violet and cyan represent C, O, P, Ni, Fe and Mo atoms, respectively. (b) The 3D differential charge density of NiFe-PMA/CNTs catalyst. The green symbols represent a decrease in charge density, while the yellow symbols represent an increase in charge density. (c) The charge of Ni and Fe atoms on NiFe/CNTs and NiFe-PMA/CNTs from bader charge analysis. (d) The chemical valence state of Ni and Fe atoms on NiFe/CNTs and NiFe-PMA/CNTs from bader charge analysis.

PMA to the NiO or FeO by metal-O bonds, resulting in increased charge density of Ni and Fe, which is consistent with the results from XPS and XAFS (Figure 2). The charge transfers between PMA and NiFe demonstrate the robust interaction existing between them. Then, the charge transfers between the PMA and NiFe were investigated further by bader charge analysis. As shown in Figure 4c, the charges of Ni and Fe on NiFe-PMA/CNTs (9.01 and 6.63, respectively) are higher than those of NiFe/CNTs (8.81 and 6.37, respectively). The oxidation states of Ni and Fe from the bader charge analysis were calculated and depicted in Figure 4d. It manifests the Ni and Fe atoms in NiFe-PMA/CNTs (0.99 and 1.37, respectively) have lower chemical valence states than those of NiFe/CNTs (1.19 and 1.63, respectively), which is consistent with XPS and XAFS results. Accordingly, the redistribution of electron density can promote the absorption of metal centers to intermediate species and optimize the catalytic performances of the electrocatalyst. [25, 26]

In summary, PMA was introduced as a promoter to enhance the NiFe oxyhyroxide for the OER in alkaline media. The constructed homogeneous/heterogeneous hybrid catalyst exhibits superior catalytic activity for OER, with a low overpotential of 203 mV as 10 mA cm^{-2} and a high TOF of 2.34 s^{-1} at 1.53 V. The incorporation of PMA induces the electronic interaction between Ni, Fe and Mo sites, as revealed by a variety of characterizations and DFT calculations, which regulate the electronic structure of NiFe, and improve the catalytic performances for the hybrid electrocatalyst. The introduction of PMA not only enhances the activity of NiFe catalyst but also maintains the high stability of the catalyst for OER, delivering a high stability of 100 h at 10 mA cm^{-2} without prominent decay. This work provided a new pathway for synthesizing and application of metal-POM hybrids for high-performance electrocatalysis.

Data availability

The data supporting this article have been included as part of the Supplementary Information.

Conflicts of interest

There are no conflicts to declare.

References

1 I. Roger, M. A. Shipman and M. D. Symes, *Nat. Rev. Chem.*, 2017, **1**, 0003.
2 J. Kibsgaard and I. Chorkendorff, *Nat. Energy*, 2019, **4**, 430-433.
3 M. Elmaalouf, M. Odziomek, S. Duran, M. Gayrard, M. Bahri, C. Tard, A. Zitolo, B. Lassalle-Kaiser, J.-Y. Piquemal, O. Ersen, C. Boissiere, C. Sanchez, M. Giraud, M. Faustini and J. Peron, Nat. Commun., 2021, **12**. 3935.
4 C. Wang, Q. Geng, L. Fan, J.-X. Li, L. Ma and C. Li, Nano Research Energy, 2023, **2**, e9120070.
5 Z. W. Seh, J. Kibsgaard, C. F. Dickens, I. Chorkendorff, J. K. Nørskov and T. F. Jaramillo, *Science*, 2017, **355**, eaad4998.
6 F. Lyu, Q. Wang, S. M. Choi and Y. Yin, *Small*, 2019, **15**, 1804201.
7 C. Wang, H. Yang, Y. Zhang and Q. Wang, *Angew. Chem. Int. Ed.*, 2019, **58**, 6099-6103.
8 Y. Sun, R. Li, X. Chen, J. Wu, Y. Xie, X. Wang, K. Ma, L. Wang, Z. Zhang, Q. Liao, Z. Kang and Y. Zhang, *Adv. Energy Mater.*, 2021, **11**, 2003755.
9 B. You, M. T. Tang, C. Tsai, F. Abild-Pedersen, X. Zheng and H. Li, *Adv. Mater.*, 2019, **31**, 1807001.
10 D. Yan, Y. Li, J. Huo, R. Chen, L. Dai and S. Wang, *Adv. Mater.*, 2017, **29**, 1606459.
11 C. Andronescu, S. Barwe, E. Ventosa, J. Masa, E. Vasile, B. Konkena, S. Moller and W. Schuhmann, *Angew. Chem. Int. Ed.*, 2017, **56**, 11258-11262.
12 X. Zhao, P. Pachfule, S. Li, J. R. J. Simke, J. Schmidt and A. Thomas, *Angew. Chem. Int. Ed.*, 2018, **57**, 8921-8926.
13 Y. Zhao, X. Jia, G. Chen, L. Shang, G. I. N. Waterhouse, L.-Z. Wu, C.-H. Tung, D. O'Hare and T. Zhang, *J. Am. Chem. Soc.*, 2016, **138**, 6517-6524.
14 L. D. Wickramasinghe, R. Zhou, R. Zong, P. Vo, K. J. Gagnon and R. P. Thummel, *J. Am. Chem. Soc.*, 2015, **137**, 13260-13263.
15 L. Wang, L. Duan, R. B. Ambre, Q. Daniel, H. Chen, J. Sun, B. Das, A. Thapper, J. Uhlig, P. Dinér and L. Sun, *J. Catal.*, 2016, **335**, 72-78.
16 S. H. Talib, Z. Lu, X. Yu, K. Ahmad, B. Bashir, Z. Yang and J. Li, *Acs Catal.*, 2021, **11**, 8929-8941.
17 K. Xia, K. Yamaguchi and K. Suzuki, *Angew. Chem. Int. Ed.*, 2023, **62**, e202214506.
18 B. Zhang, H. Asakura, J. Zhang, J. Zhang, S. De and N. Yan, *Angew. Chem. Int. Ed.*, 2016, **55**, 8319-8323.
19 F. M. Toma, A. Sartorel, M. Iurlo, M. Carraro, P. Parisse, C. Maccato, S. Rapino, B. Rodriguez Gonzalez, H. Amenitsch, T. Da Ros, L. Casalis, A. Goldoni, M. Marcaccio, G. Scorrano, G. Scoles, F. Paolucci, M. Prato and M. Bonchio, *Nat. Chem.*, 2010, **2**, 826-831.
20 G. Y. Lee, I. Kim, J. Lim, M. Y. Yang, D. S. Choi, Y. Gu, Y. Oh, S. H. Kang, Y. S. Nam and S. O. Kim, *J. Mater. Chem. A*, 2017, **5**, 1941-1947.
21 Q. Zhang, C. Yue, Q. Pu, T. Yang, Z. Wu and Y. Zhang, *Acs Omega*, 2019, **4**, 9041-9048.
22 M. Gao, W. Sheng, Z. Zhuang, Q. Fang, S. Gu, J. Jiang and Y. Yan, *J. Am. Chem. Soc.*, 2014, **136**, 7077-7084.
23 S. V. B. Billy B. Bardin, Matthew Neurock, Robert J. Davis, *J. Phys. Chem. B*, 1998, **102**, 10817-10825.
24 Z. Cai, P. Wang, J. Zhang, A. Chen, J. Zhang, Y. Yan and X. Wang, *Adv. Mater.*, 2022, **34**, 2110696.
25 I. C. Man, H.-Y. Su, F. Calle-Vallejo, H. A. Hansen, J. I. Martinez, N. G. Inoglu, J. Kitchin, T. F. Jaramillo, J. K. Norskov and J. Rossmeisl, *Chemcatchem*, 2011, **3**, 1159-1165.
26 C. Liang, R. R. Rao, K. L. Svane, J. H. L. Hadden, B. Moss, S. B. Scott, M. Sachs, J. Murawski, A. M. Frandsen, D. J. Riley, M. P. Ryan, J. Rossmeisl, J. R. Durrant and I. E. L. Stephens, *Nat. Catal.*, 2024, DOI: 10.1038/s41929-024-01168-7.

The data availability statement

The data supporting this article have been included as part of the Supplementary Information.

ChemComm Accepted Manuscript